


Article

# Fabrication, Morphology Analysis, and Mechanical Properties of Ti Foams Manufactured Using the Space Holder Method for Bone Substitute Materials

Okтай Cetinel <sup>1,\*</sup> , Ziya Esen <sup>2</sup> and Bora Yildirim <sup>1</sup>

<sup>1</sup> Department of Mechanical Engineering, Hacettepe University, Ankara 06800, Turkey; boray@hacettepe.edu.tr

<sup>2</sup> Department of Materials Science and Engineering, Cankaya University, Ankara 06790, Turkey; ziyaesen@cankaya.edu.tr

\* Correspondence: oktaycetinel@hacettepe.edu.tr; Tel.: +90-312-418-4129

Received: 15 February 2019; Accepted: 13 March 2019; Published: 17 March 2019



**Abstract:** Porous titanium (Ti) offers several key attributes as a biomedical material. Among the known characteristics of Ti relevant to biomedical applications, the mechanical performance and effects of a pore structure on the deformation characteristics under compressive loading were examined. The space holder method was employed to generate Ti foams with target porosities of 60%, 70%, and 80%. A micro-computed tomography analysis and light and scanning electron microscopy were performed to examine the pore morphology and microstructure. The mechanical properties along with the elastic modulus and compressive strength were evaluated via uniaxial compression testing. Ti foam samples with three porosity levels displayed average elastic moduli and compressive strengths comparable with those of human cancellous and cortical bone. All the Ti foam samples had elastic moduli similar to those of cancellous bone with their open porous structures. Although the foam samples with ~60% porosity had compressive strength comparable to that of cortical bone, the samples with ~80% porosity displayed compressive strength similar to that of cancellous bone. The results indicate that Ti foam scaffolds produced using the space holder method have great potential for applications in hard tissue engineering, as their mechanical properties and pore structures are similar to those of bone.

**Keywords:** biomaterials; Ti foam; micro-CT analysis; mechanical properties

## 1. Introduction

The superior biocompatibility, specific strength, and corrosion resistance of titanium (Ti) and its alloys have led to the extensive use of these materials in bone implants [1–3]. A major problem with such implants is stress shielding due to the difference between the elastic moduli of implant materials (110 GPa for Ti) and that of bone (10–30 GPa). This difference leads to delayed bone healing, increased porosity in the bone surrounding the implant, and loosening of the implant [4,5]. These issues have generated growing interest in the development of metallic implant materials with reduced elastic moduli.

In particular, porous materials have attracted increasing research interest as potential orthopedic materials with well-matched elastic moduli that permit long-term bonding via full in-growth of the bone tissues [6–8]. Various porous materials have been discussed in numerous published reviews focused on the importance of both mechanical and microscopic structural properties (pore size and porosity) [8–10]. In particular, the significance of these morphological properties for achieving bone regeneration via osteogenesis has been discussed [11]. While significant bone in-growth was reported for large pore sizes of 100–600  $\mu\text{m}$ , small pore sizes of 75–100  $\mu\text{m}$  show unmineralized osteoid tissue

growth, and 10–75  $\mu\text{m}$  pores exhibit fibrous tissue growth [12,13]. Hence, 100  $\mu\text{m}$  is usually regarded as the minimum pore size for successful mineralized bone regeneration [14–18].

Porous Ti scaffolds can be produced using several methods, such as additive manufacturing, foaming, and powder metallurgy. The economy and high efficiency of powder metallurgy have resulted in broad industrial applications in material blending and compaction, facilitating the mass production of implant materials with tailored compositions, shapes, and mechanical properties [19]. Moreover, powder sintering in combination with space holder techniques can generate highly porous scaffolds with effective control of the morphology. Many authors have described this approach, in which the metallic powders and space holder particles are mixed together and compacted prior to the removal of the space holders either before or during sintering [14–16]. Magnesium (Mg) has also been reported to be a potential space holder material for fabricating porous scaffolds of Ti [2].

The porosity, pore size, and morphology of the resulting material determine its mechanical properties. Hence, numerous researchers have examined the effects of various porosities and/or pore sizes on the mechanical performance of porous Ti [2,6–11]. Nevertheless, the effect of varying the pore-size distribution has not been well examined using micro-computed tomography (micro-CT) analysis [20].

In the present study, Mg powder was used as a space holder in a powder metallurgical approach to produce porous Ti scaffolds for applications in tissue engineering. The aim was to produce metallic scaffolds with interconnected pore structures along with mechanical characteristics compatible with those of human cancellous and cortical bones. The deformation behaviors of the manufactured Ti foams were investigated under quasi-static compression conditions, and the mechanical properties were correlated with the porosity content, pore size, and the cell wall structure.

## 2. Materials and Methods

### 2.1. Scaffold Preparation

The powder metallurgy method was used to generate porous Ti scaffolds, in which the porosity was constrained by varying the volume ratio of Mg to Ti powder. For the primary matrix, angular Ti powder (Phelly materials, >99% purity (conforming to ASTM 1580-1), Phelly materials, Upper Saddle River, NJ, USA) with particle size in the range of 50–60  $\mu\text{m}$  and an average particle size of 53.6  $\mu\text{m}$  was used. For the space holder material, Mg powder was chosen, because it has very limited solid solubility in Ti [2]. Spherical Mg powder (Tangshan Weihao Magnesium Powder Co. LTD., Tangshan, China; >99.8% purity) had an average particle size of around 300  $\mu\text{m}$  and particle size distribution between 250 and 355  $\mu\text{m}$ . The selection of Mg powder size was informed by published work in which a pore size of 250  $\mu\text{m}$  was found to assist cell migration, while optimal mechanical properties of the porous structure were achieved via high sphericity [2]. Hence, a 250  $\mu\text{m}$  pore size was the objective for optimum osteointegration performance after sintering the porous samples.

A polyvinyl alcohol (PVA, [-CH<sub>2</sub>CHOH-]<sub>n</sub>) solution was added to Ti powder and was mixed for 1 h with Mg powders to generate powder mixtures containing 60%, 70%, and 80% Mg by volume. Cylindrical samples (9 mm diameter, 9 mm height) for characterization were then produced at room temperature by uniaxial compression at 600 MPa for 20 seconds using a 12-ton capacity manual hydraulic press (Kardesler Makina) with floating die. At least four samples in each targeted porosity group were prepared using the same procedure to analyze the repeatability and accuracy of the experiments.

The samples were sintered for 2 h under flowing Ar gas (99.999%) at 1200 °C in an atmosphere-controlled tube furnace (Protherm PLF 140, Protherm, Ankara, Turkey). To avoid contamination during sintering, the samples were positioned in Ti crucibles obtained by the machining of Ti rods. To avoid adverse effects on the scaffold integrity due to melting and boiling of the Mg powders and to enable maximum removal of the space holder, the furnace was heated to the sintering temperature (above the boiling point of Mg, 1090 °C) slowly at a heating rate of 4 °C/min.

## 2.2. Morphology, Porosity, and Phase Analysis

Light microscope (Eclipse LV150N, Nikon, Tokyo, Japan) and scanning electron microscope (SEM, Jeol JSM 6400 equipped with Noran System 6 X-ray microanalysis system, Tokyo, Japan) were used to examine the morphology and microstructure of the foams. For this procedure, the specimens were crushed to observe the pore structure, and the samples were prepared metallographically after mounting, which were cut longitudinally along the axis of compaction. Kroll's reagent was used to reveal the underlying microstructures of the foams. In addition, to studying the change of the pore morphology of the specimens under compression deformation, each specimen was examined using SEM both before and after compression testing.

The internal and external pore shapes, along with the surface and volume characteristics relevant to bone histomorphometry (e.g., porosity and pore distribution), were examined by micro-CT using a Skyscan 1272 industrial micro-CT machine (Brüker, Billerica, MA, USA), affording a maximum resolution of 0.35  $\mu\text{m}$  (16 Mp). A step size of 0.01 mm was used to examine the scaffold cross-sections in three directions of at least three samples in each targeted porosity group.

ImageJ (1.52e, NIH, Bethesda, MD, USA, 2018) was used to analyze the micropore distribution patterns with the image threshold technique on SEM images to determine the overall porosity level and microporosity and to calculate the mean pore diameter equivalents, pore morphology, and sizes. Following scanning, the micrograph images underwent a cleaning process to sharpen the features, allowing for more precision and accuracy in the analysis. This stage is necessary as the program in imaging employs color threshold changes; thus, the clean image allows for closer examination of the details of the micrograph. Following image analysis, the extracted data were then stored in Microsoft Excel format to allow for additional statistical analysis and presentation in graphs. Doing so made it possible to determine the pore distribution and the relationship between the immersion period and final micropore size/structure.

The main phases in the manufactured porous samples were identified via X-ray diffraction (XRD, RigakuD/Max2200/PC, Rigaku, Tokyo, Japan) analysis at 40 kV with a scan speed of 1°/min between 30° and 90° 2 $\theta$  angles using a Cu-K $\alpha$  radiation source. On the other hand, O, H, and N contents of the as-received Ti powders and manufactured foams were measured with a LECO TCH 600 Simultaneous O, H, N Determinator, LECO, St. Joseph, MI, USA)

## 2.3. Mechanical Testing

To examine their mechanical properties, cylindrical porous Ti samples (9 mm diameter, 9 mm height) were subjected to compression testing at room temperature using an Instron 3369 (Instron, Norwood, MA, USA) with a cross head speed of 0.005 mm/s. It is known that an increase in strain rate during compression testing does not significantly affect elastic modulus, but a pronounced rise occurs in compressive strength when the strain rate is increased [8]. Therefore, the speed of testing in the present study was kept as low as possible.

To obtain the stress–strain curves of samples, each specimen was subjected to an increasing load until a complete fracture of the specimen was observed. The moduli of the samples were found by measuring the slopes of the linear regions of the curves, while the compression strengths were measured at the maximum stress levels of the stress–strain curves. The evaluated results were also compared with human cortical and cancellous bone to analyze the similarities.

## 3. Results

### 3.1. Morphology and Phase Analysis

Representative SEM images obtained from the crushed cross-sections of samples designed to have porosities near 60%, 70%, and 80% are shown in Figure 1. After Mg removal by evaporation, the samples with target porosities of 60%, 70%, and 80% were observed to have porosities in the ranges of 55.9–62.9%, 65.6–69.9%, and 74.0–78.0%, respectively. The small discrepancies between the target and

obtained porosity levels were attributed to sintering, which resulted in the shrinkage of the samples by the formation of sintering bonds between the particles. In the samples with relatively low additions of Mg particles, i.e., 60% Mg, the pore shapes were usually round with smoothly curved pore walls. For higher porosity levels, the pore shape started to deviate from a perfect spherical shape probably due to pore interconnections.

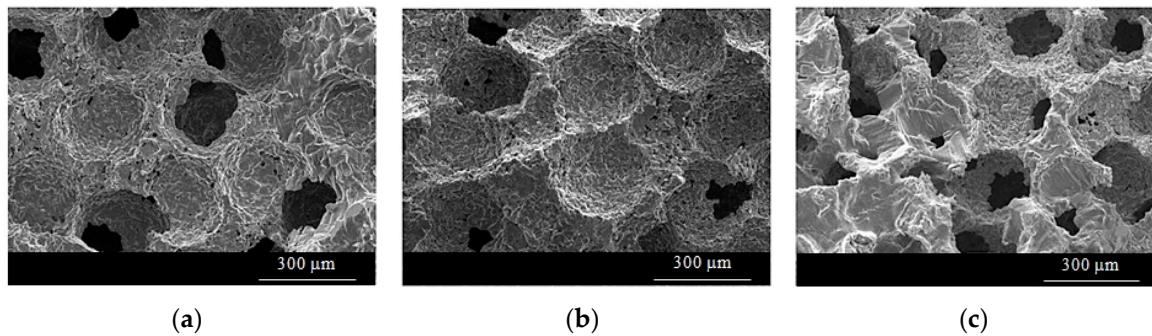


**Figure 1.** SEM macrostructure of porous Ti samples at  $\times 100$  magnification with porosities of (a) 55.9%, (b) 68.4%, and (c) 78%.

Along with the large macropores generated by removing the Mg particles, Figure 2 also reveals the presence of micropores on the cell walls due to incomplete sintering of the Ti powders. This characteristic is typical of sintered Ti microstructures. Although the cell walls were microporous, the sintering was sufficient to form bonds between the Ti powders, as revealed by the grain boundaries of  $\alpha$ -Ti in Figure 2b.

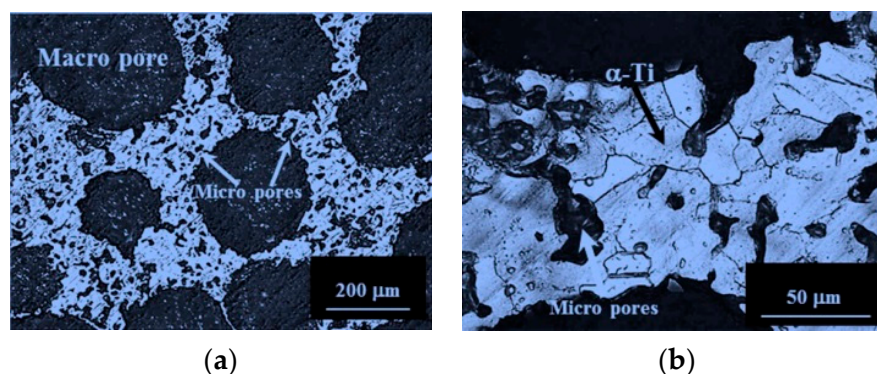


**Figure 2.** Polished cross-sectional light microscope images of Ti foam with 55.9% porosity showing (a) macropores formed by Mg evaporation and microporous cell walls and (b) cell walls containing micropores and grains of the  $\alpha$ -Ti phase.

The micro-CT scan images for the samples in three different porosity contents are shown in Figure 3.

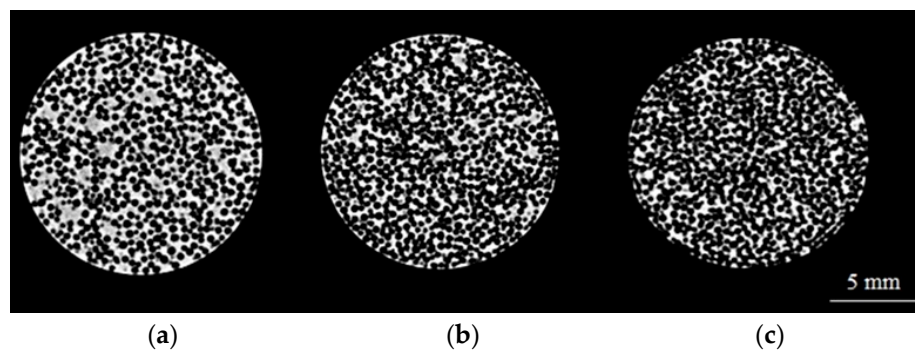


**Figure 3.** Micro-CT scan microstructure of porous Ti samples with porosities of (a) 55.9%, (b) 68.4%, and (c) 78.0%.

The micro-CT scans indicated a significant level of agreement between the target and the obtained porosities. The average resultant pore diameters, measured using imageJ software, were around 253, 267, and 273  $\mu\text{m}$  for the samples with porosities in the range of 55.9–58.7%, 68.4–69.9%, and 76.4–78.0%, respectively (Figure 4). As can be seen, the obtained average pore sizes in all the samples were less than the initial average Mg particle size (300  $\mu\text{m}$ ), probably due to sintering shrinkage, which caused further densification by formation of sintering bonds. The average pore size was observed to increase with the increasing Mg content of the initial compacts, because more interconnections occurred between the pores after removing Mg from these samples (Figure 3c).

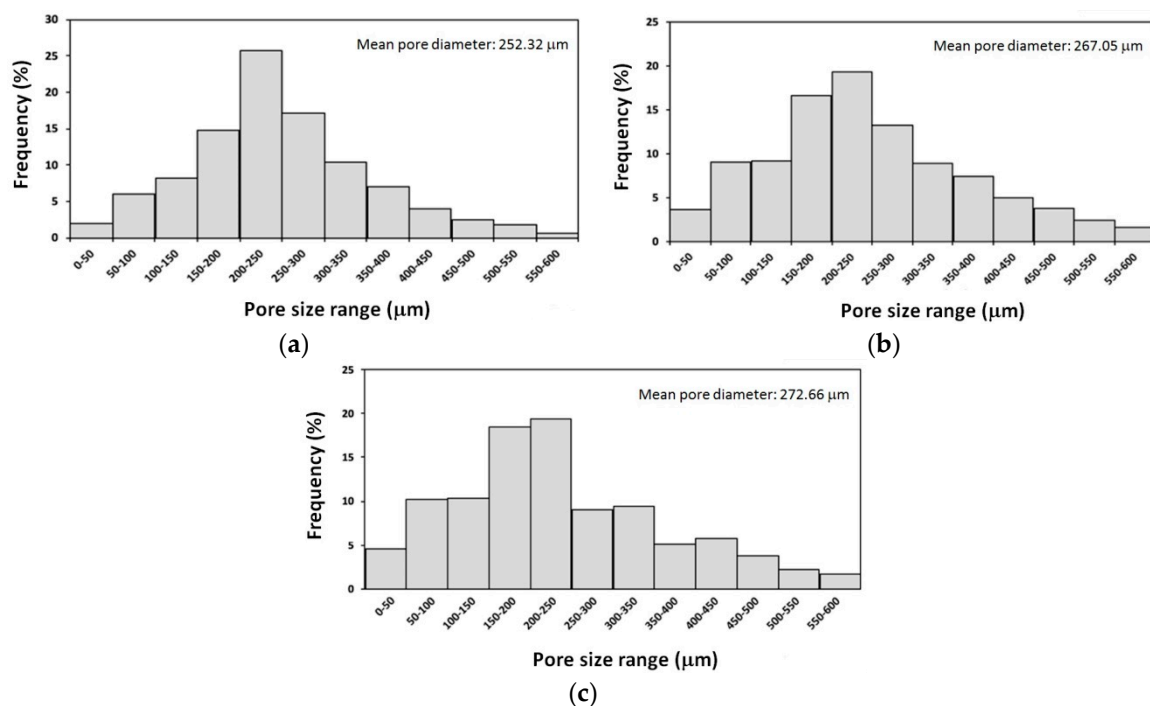


**Figure 4.** Porosity analysis results obtained using an imageJ image analyzer from three samples in each porosity range of (a) 55.9–58.7%, (b) 68.4–69.9%, (c) 76.4–78.0%.

According to the statistical pore-size analysis results (Figure 4), the Ti samples had pore sizes in the range of 5.0–887.5  $\mu\text{m}$ . The pores larger than the initial Mg particles were due to the interconnection of large pores. Meanwhile, the pores smaller than the Mg particles, called micropores, were likely due to partial sintering of Ti powders on the cell walls, as shown in Figure 2. Further, all of the samples displayed largely uniform pore size distributions in the range of 150–300  $\mu\text{m}$  with good, open porous structures, both in their surface and interior regions.

In addition to the porosity content and the morphologies and type of pores, the production of Ti foams free of oxides and without binder residue or Mg is crucial for biomedical applications. In all of the samples, Mg was completely removed during production, so the manufactured foams were free of binder residue and Mg, as can be seen in the X-ray diffraction patterns in Figure 5 and EDS analysis given in Figure 6. Moreover, no oxides of Ti were detected and the production technique yielded only the  $\alpha$ -Ti phase, as revealed by the  $\alpha$ -phase grains in Figure 2b and the diffraction patterns. However, production caused an increase in the dissolved contents of interstitial elements (oxygen, hydrogen, and nitrogen) probably due to flowing argon gas during foam production. Although argon gas was highly pure (99.999%), it contained oxygen, nitrogen, and water vapor in ppm and vpm levels, respectively. Therefore, the increase in the impurity levels of the samples was attributed to oxygen, nitrogen, and water vapor coming from argon gas, which flowed over the samples at a rate of 10 L/h throughout the experiment (Table 1).

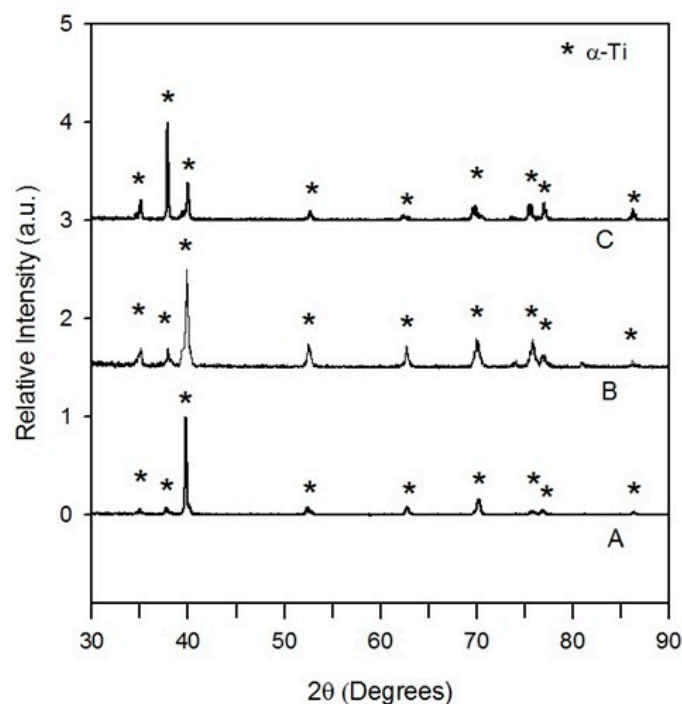


**Figure 5.** X-ray diffraction patterns of manufactured Ti foams. A: 55.9% porosity, B: 68.4% porosity, and C: 78.0% porosity.

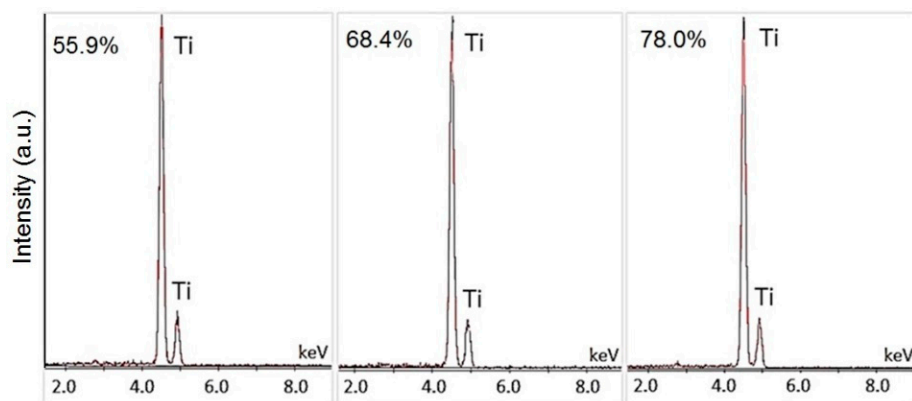


**Figure 6.** EDS analysis of manufactured foam samples with three different porosity contents (55.9%, 68.4%, and 78.0%).

**Table 1.** Average O, H, and N contents of starting Ti powders and manufactured Ti foams.

Element	As-Received Ti powder	Ti Foams
Oxygen (wt.%)	0.048	0.207
Hydrogen (wt.%)	0.0038	0.0626
Nitrogen (wt.%)	0.0013	0.0980

### 3.2. Mechanical Properties

#### 3.2.1. Stress–Strain Curves

The compressive stress–strain curves of the Ti samples with different porosity groups are presented in Figure 7. The curves show an initial elastic deformation phase followed by an extensive plateau with almost constant flow stress up to significant strains. The stress–strain curves of such foams also contain a densification stage, in which the flow stress increases sharply. However, this stage could not be observed in the given curves, because the samples fractured at the beginning of the densification stage. This type of behavior has also been widely observed in Ti foams in previous research studies [11–15].

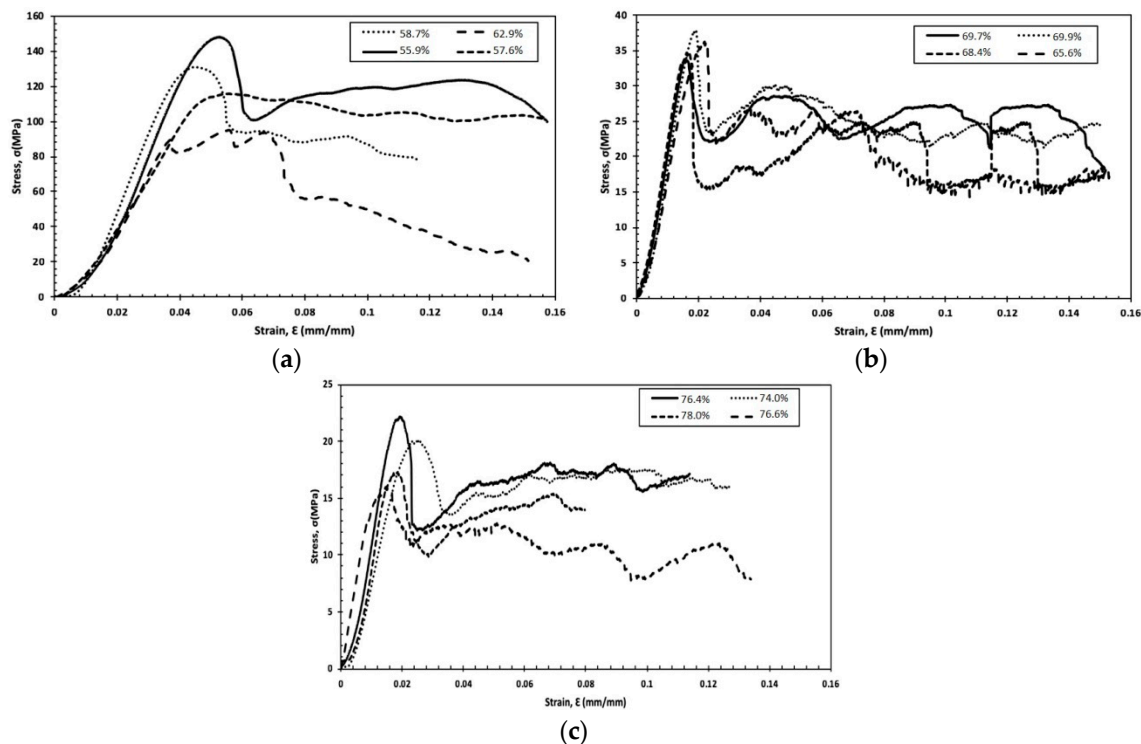


**Figure 7.** Compressive stress–strain curves of porous Ti samples with three different porosity ranges; (a) 55.9–62.9%, (b) 65.6–69.9%, and (c) 74.0–78.0%.

All the plateau regions were observed following maximum peak stresses, which suddenly dropped prior to the start of the plateau stage. The maximum peak compressive strengths were found to be around 148.0 MPa, 38.0 MPa, and 22.0 MPa, while their lowest values at the drop point were around 92.0 MPa, 34.0 MPa, and 16.0 MPa for the porous samples given in Figure 7a–c, respectively.

The elastic moduli of the Ti group samples with different porosity contents are presented in Figure 8a. In the present study, the elastic moduli were obtained from the slopes of the linear elastic regions after subtracting the testing machine stiffness. Thus, for the first group of samples (55.9–62.9% porosity), the elastic moduli were 3.1–4.5 GPa, while the second group of samples (65.6–69.9% porosity) had elastic moduli of 2.6–2.8 GPa, and the third group of samples (74.0–78.0% porosity) displayed

elastic moduli in the range of 1.2–1.65 GPa. The elastic modulus generally increased with decreasing porosity, with the maximum elastic modulus of 4.5 GPa being measured for the sample with 58.7% porosity. When the porosity was increased to 78.0%, the elastic modulus was reduced to just 1.2 GPa. This trend held true for the samples having porosities between the maximum and minimum porosities, as they displayed elastic moduli less than or equal to 2.8 GPa. The mean elastic moduli were calculated to be 3.9, 2.7, and 1.45 GPa for the first, second, and third group of samples, respectively. The calculated elastic moduli of the foams fall in the range of that of human cancellous bone (0.5–5 GPa) [21], which has an open porous structure similar to those of manufactured Ti foams. Therefore, manufactured foams may be evaluated as potential candidate biometals, as they have elastic moduli similar to those of bone, which helps alleviate stress shielding. However, most of the bones are composed of both cortical bone shell and cancellous core. The elastic modulus of the human jaw bone with a similar structure, for example, changes between 15 and 18 GPa [22], which is above the elastic moduli of the manufactured composites. In this case, the porosity content of foams should be decreased or a biocompatible titanium alloy grade with higher elastic modulus should be chosen in foam production to have a similar elastic modulus to that of jaw bone.

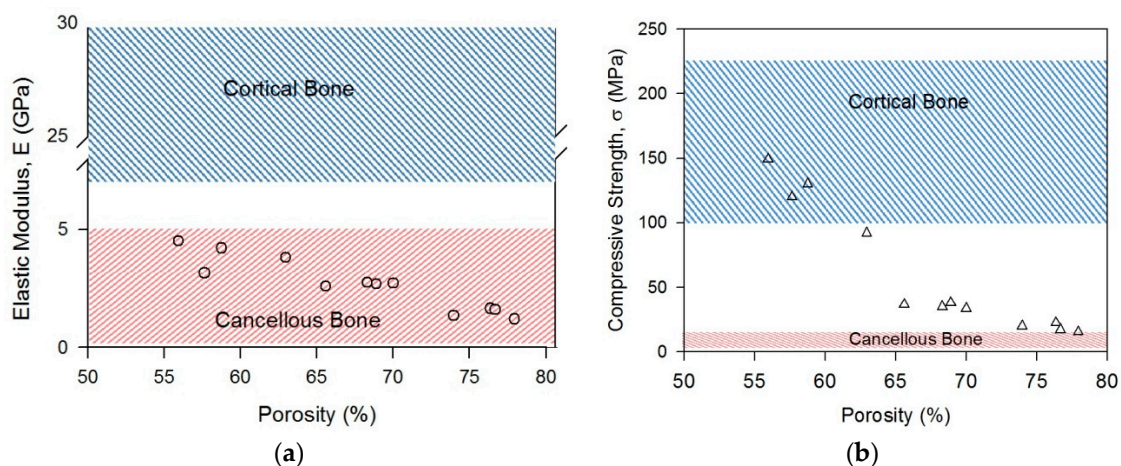


**Figure 8.** Mechanical properties changes of Ti foams with different porosities: (a) elastic modulus, (b) compressive strength.

Similar to the elastic modulus versus porosity change, the compressive strength (peak stress measured subsequent to the elastic region) displayed a decreasing tendency with increasing porosity. However, the strength drop beyond 60% porosity was rather sharp (Figure 8b). Although the samples in the first group (55.9–62.9% porosity) had compressive strengths in the range of cortical bone strength (100–230 MPa [21]), those in the third group (74.0–78.0% porosity) had strengths close to that of cancellous bone 2–12 MPa [21]. Meanwhile, the samples in the second group (65.6–69.9%) exhibited compressive strengths between those of cortical and cancellous bone. It is clearly evident that, by alternating the porosity content, it is possible to tune the mechanical properties of foams to make them mechanically more compatible with human bone.

Implants made of bulk materials with greater elastic moduli and compressive strengths than bone do not permit the necessary transfer of stress to the neighboring bone. This situation promotes resorption of the bone surrounding the implant, thereby loosening the implant, reducing the service life, and ultimately requiring revision surgery. Hence, materials with mechanical properties more comparable to those of human bone (i.e., high strength and low elastic modulus) are necessary if these problems are to be avoided [13]. The porous Ti samples manufactured in the present study displayed compressive strengths and elastic moduli comparable with those of human bone, demonstrating the potential application of these materials in biomedical implants.



### 3.2.2. Macroscopic Deformation Band

As can be seen in Figure 7, titanium foams experienced different deformation modes up to fracture point. Each dominant deformation mode in each stage changes the shape of foams on the macro- and microscale, either permanently or temporarily. It is known that bending in cell edges of the foam in the linear elastic region is the dominant mechanism in open porous structures, and it does not change the sample's shape permanently [23]. However, permanent deformation and shape changes occur when the stress in the walls and the edges of the foam exceed the yield stress. Therefore, in addition to the porosity content and pore size, features of cell wall and edges, i.e., their thickness, is crucial in determining the mechanical responses. The struts in the manufactured foams of the present study had an hour-glass shape (Figure 2a), such that the material was concentrated at cell nodes and the thickness of the cell walls and edges were observed to decrease from the cell node to the center. Additionally, the struts were not fully dense, and they contained micropores left from partial sintering. According to minimum solid area (MSA) models [24], the minimum solid cross-sectional area, i.e., the area normal to the stress, is assumed to dominate in the transmission of stress. Currently mechanical models developed for various foam structures are essentially specialized MSA models. Properties and dimensions of the struts or webs between the pores and the sintering degree of the cell walls play an important role in the mechanical properties, because elastic and plastic deformation localize at those points.

In the present study, subsequent to the end of the linear elastic region, deformation bands perpendicular to the loading direction developed, in which plastic collapse of some cells took place. This effect was accompanied by the beginning of the plateau region by a sudden drop in flow stress (Figure 7). With increasing strain in the plateau region, additional deformation bands were formed during plateau stage. An investigation of the deformation bands under a microscope revealed cracks along the microporous cell walls, which are actually the minimum solid area regions of the titanium foams. Although the deformation bands observed on the macroscale were perpendicular to the deformation axis, cracking was observed to occur in different directions, as shown by the arrows in Figure 9. Possibly, the weakest cell wall at different angles served as the initiation site for strain localization. Once collapsing completed in one region, deformation continued with the new band formation at different locations by deformation and cracking of the weaker cell walls.

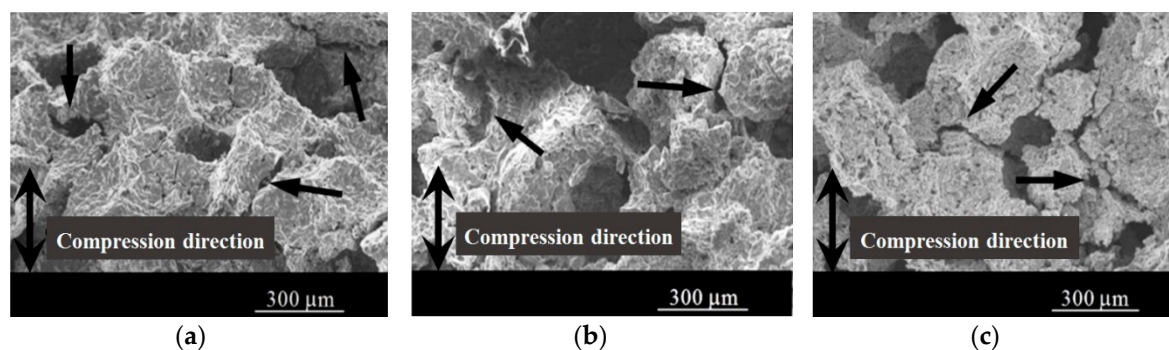


**Figure 9.** SEM images of compressed porous Ti samples with different porosities at  $\times 100$  magnification; (a) 57.6%, (b) 69.7%, and (c) 78.0%.

### 3.2.3. Microscopic Deformation Mode of Cell Wall

As mentioned previously, the foam samples were deformed permanently by the formation of deformation bands, which are supposed to occur due to localized deformation at cell walls as a result of cell wall buckling, bending, and yielding according to previous works [23]. In fact, the structure (cell wall thickness and shape, presence of defects such as micropores, underlying microstructure) and inherent mechanical properties of the cell walls affects the deformation mechanisms encountered during compression loading. For example, the presence of micropores in cell walls creates stress

concentrations due to sharp curvatures at the neck regions of the partially sintered powders and causes early deformation. Additionally, deformation in cell walls localizes in the neck regions of the sintered powders, which are actually the minimum solid area regions of each cell wall. Similarly, an examination of deformation bands in cell walls in a higher magnification revealed micro cracks mostly along the sintering necks (Figure 10). Although it was not very common, cracking was also detected across the titanium powders, similar to transgranular brittle fracture. This type of fracture seen along the powders in the present study were attributed to local oxidation of some regions during sintering, which highly influences the ductility and strength of titanium samples. Therefore, chemical composition or inherent properties of the cell wall material may also be dominant in determining the deformation mode at the microscale and should be considered when developing a micro-mechanical model.

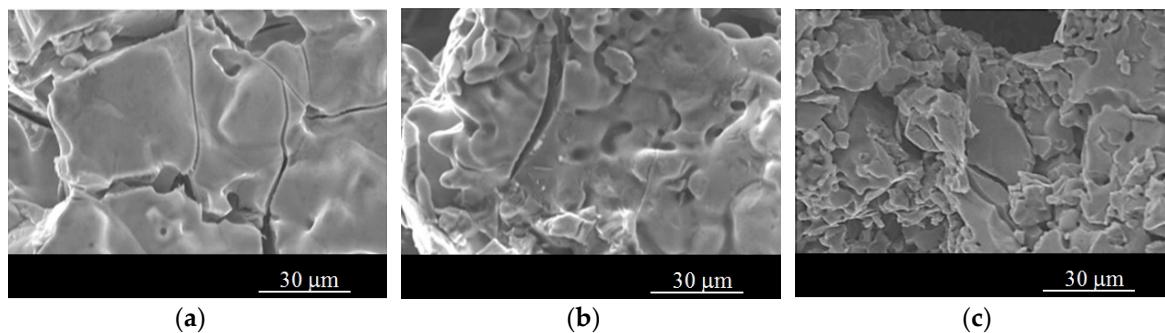


**Figure 10.** SEM images of compressed porous Ti samples with different porosities at  $\times 1000$  magnification; (a) 57.6%, (b) 69.7%, and (c) 78.0%.

## 4. Discussion

### 4.1. Structure Observation

Previous studies, both in vivo and in vitro, have shown that the desirable pore size of biomaterials is one of the key parameters in the process of bone development [5]. In the present study, the analysis indicated that the target porosity range of 150–300  $\mu\text{m}$  was attained, with a uniform, narrow distribution of pores ( $256 \mu\text{m} \pm 28 \mu\text{m}$ ) displaying high levels of interconnectivity from the center to the surface of the material. According to previous research, this pore morphology promotes osseointegration by aiding the transport of oxygen and nutrients necessary for the formation of blood vessels during the development of bone tissue [8]. Two types of pores were present in the Ti samples: (i) large or macro pores (100–350  $\mu\text{m}$ ), which promote direct bone formation, and (ii) small or micro pores (<100  $\mu\text{m}$ ), which promote hypoxic conditions and stimulate the formation of articular cartilage prior to bone formation. Hence, previous researchers have argued that porous Ti with this type of connective three-dimensional network morphology could benefit bone formation, as well as supplying pathways for effective in-growth of bone [8].

### 4.2. Mechanical Properties

The presently available bulk implant materials display greater stiffness than human bone, thereby failing to transfer the requisite amount of stress to the surrounding bone. This shortcoming leads to implant loosening due to resorption of the bone surrounding the implant. Consequently, the development of implant materials with optimum combinations of compressive strength and low elastic modulus are necessary to prevent implant loosening, increase implant service life, and circumvent the need for surgical readjustment [5]. The elastic modulus of human cortical bone is in the range of 7–30 GPa, while that of human cancellous bone is less than 5 GPa [21], and the compressive strength of human bone ranges from 2 to 230 MPa [21]. In the present study, the Ti foam samples displayed decreasing compressive strengths of 149–15 MPa and elastic moduli of 4.5–1.2 GPa with increasing porosity. Thus, porous Ti materials with broad ranges of compressive strengths and elastic moduli are

desirable equivalents to human bone, making Ti foams promising choices for biomedical applications. However, in addition to elastic modulus and strength, the fracture toughness of the titanium foams is an important property that needs to be investigated. Fracture toughness testing of foam samples can be carried out in the opening mode of (mode I) loading using pre-cracked samples [25], and the fracture toughness of the titanium itself in the cell walls of foams may be calculated by pillar splitting method [26], which makes use of micro-pillars of materials that are loaded to fracture by nano-indentation. The KIC (plane strain fracture toughness) values of cancellous bone and cortical bone are reported to be  $1.5 \text{ MNm}^{-3/2}$  [27] and  $3.5 \text{ MNm}^{-3/2}$  [28], respectively. Accordingly, the porosity content, pore shape, and the cell wall structure of the foams should be precisely controlled, together with the intrinsic material properties of cell walls (i.e., purity), to have fracture toughness values close to bone.

## 5. Conclusions

In the present study, the space holder powder metallurgy technique was used in combination with a Mg powder space holder to produce biomimetic Ti scaffolds with selected porosities (60%, 70%, and 80%). Each porous scaffold displayed a significant degree of pore interconnectivity, which is favorable for osseointegration and in-growth of bone tissue. A porosity analysis also indicated that an appropriate pore size range was achieved for promoting osseointegration, as defined in the previous literature [12,13]. Moreover, the first group (55.9–62.9% porosity) and third group samples (74.0–78.0% porosity) samples displayed compressive strengths compatible with those of human cortical and cancellous bone. Meanwhile, all the foam samples exhibited elastic moduli similar to that of cancellous bone. Hence, the combined results of the structural and mechanical analyses performed in this study suggest that Ti scaffolds manufactured using the described approach could be promising materials for applications in bone tissue engineering.

**Author Contributions:** Z.E. conceived of and designed the experiments; O.C. performed the experiments and analyzed the data; O.C. conducted the compression tests; B.Y. provided porosity analysis using ImageJ software; O.C. and B.Y. wrote the paper; and O.C. and Z.E. revised the paper. The research project was supervised by B.Y. and Z.E.

**Funding:** This research received no external funding.

**Acknowledgments:** This work was conducted at the Joint-Use Facilities Laboratory of Mechanical Material Test Analysis and SEM Characterisation Lab at Hacettepe University and Biomaterials Lab at Cankaya University.

**Conflicts of Interest:** The authors declare no conflict of interest.

## References

1. Singh, R.; Lee, P.D.; Jones, J.R.; Poologasundarampillai, G.; Post, T.; Lindley, T.C.; Dashwood, R.J. Hierarchically structured titanium foams for tissue scaffold applications. *Acta Biomater.* **2010**, *6*, 4596–4604. [[CrossRef](#)] [[PubMed](#)]
2. Esen, Z.; Bor, Ş. Characterization of Ti-6Al-4V alloy foams synthesized by space holder technique. *Mater. Sci. Eng. A* **2011**, *528*, 3200–3209. [[CrossRef](#)]
3. Kashef, S.; Asgari, S.A.; Hodgson, P.; Yan, W.Y. Simulation of Three-Point Bending Test of Titanium Foam for Biomedical Applications. *Adv. Mater. Res.* **2008**, *32*, 237–240. [[CrossRef](#)]
4. Imwinkelried, T. Mechanical properties of open-pore titanium foam. *J. Biomed. Mater. Res. Part A* **2007**, *81*, 964–970. [[CrossRef](#)] [[PubMed](#)]
5. Matsushita, T.; Fujibayashi, S.; Kokubo, T. Titanium foam for bone tissue engineering. *Met. Foam Bone Process. Modif. Charact. Prop.* **2016**, *17*, 111–130.
6. Barrabés, M.; Sevilla, P.; Planell, J.A.; Gil, F.J. Mechanical properties of nickel-titanium foams for reconstructive orthopaedics. *Mater. Sci. Eng. C* **2008**, *28*, 23–27. [[CrossRef](#)]
7. Kato, K.; Ochiai, S.; Yamamoto, A.; Daigo, Y.; Honma, K.; Matano, S.; Omori, K. Novel multilayer Ti foam with cortical bone strength and cytocompatibility. *Acta Biomater.* **2013**, *9*, 5802–5809. [[CrossRef](#)]

8. Tuncer, N.; Arslan, G. Designing compressive properties of titanium foams. *J. Mater. Sci.* **2009**, *44*, 1477–1484. [[CrossRef](#)]
9. Xue, X.B.; Zhao, Y.Y.; Kearns, V.; Williams, R.L. Mechanical and Biological Properties of Titanium Syntactic Foams. *Miner. Met. Mater. Soc.* **2010**, *2*, 129–136.
10. Mansourighasri, A.; Muhamad, N.; Sulong, A.B. Processing titanium foams using tapioca starch as a space holder. *J. Mater. Process. Technol.* **2012**, *212*, 83–89. [[CrossRef](#)]
11. Kashef, S.; Asgari, A.; Hilditch, T.B.; Yan, W.; Goel, V.K.; Hodgson, P.D. Fatigue crack growth behavior of titanium foams for medical applications. *Mater. Sci. Eng. A* **2011**, *528*, 1602–1607. [[CrossRef](#)]
12. Jian, X.; Hao, C.; Qiu, G.; Yang, Y.; Lyu, X. Investigation on relationship between porosity and spacer content of titanium foams. *Mater. Des.* **2015**, *88*, 132–137. [[CrossRef](#)]
13. Ahmad, S.; Kassim, A. Fabrication of titanium foam by using compaction method. In Proceedings of the 26th Regional Conference on Solid State Science & Technology 2011, Negeri Sembilan, Malaysia, 22–24 November 2011.
14. Spoerke, E.D.; Murray, N.G.; Li, H.; Brinson, L.C.; Dunand, D.C.; Stupp, S.I. A bioactive titanium foam scaffold for bone repair. *Acta Biomater.* **2005**, *1*, 523–533. [[CrossRef](#)] [[PubMed](#)]
15. Xiong, J.Y.; Li, Y.C.; Wang, X.J.; Hodgson, P.D.; Wen, C.E. Titanium-nickel shape memory alloy foams for bone tissue engineering. *J. Mech. Behav. Biomed. Mater.* **2008**, *1*, 269–273. [[CrossRef](#)]
16. Xiao, J.; Yang, Y.; Qiu, G.B.; Liao, Y.L.; Cui, H.; Lü, X.W. Volume change of macropores of titanium foams during sintering. *Trans. Nonferrous Met. Soc. Chin. (Engl. Ed.)* **2015**, *25*, 3834–3839. [[CrossRef](#)]
17. Li, J.P.; Li, S.H.; de Groot, K.; Layrolle, P. Preparation and Characterization of Porous Titanium. *Key Eng. Mater.* **2001**, *218–220*, 51–54. [[CrossRef](#)]
18. Xie, B.; Fan, Y.Z.; Mu, T.Z.; Deng, B. Fabrication and energy absorption properties of titanium foam with CaCl<sub>2</sub> as a space holder. *Mater. Sci. Eng. A* **2017**, *708*, 419–423. [[CrossRef](#)]
19. Bansiddhi, A.; Dunand, D.C. *Titanium and NiTi Foams for Bone Replacement*; Woodhead Publishing Limited: Cambridge, UK, 2014; ISBN 9780857099037.
20. Sargeant, T.D.; Guler, M.O.; Oppenheimer, S.M.; Mata, A.; Satcher, R.L.; Dunand, D.C.; Stupp, S.I. Hybrid bone implants: Self-assembly of peptide amphiphile nanofibers within porous titanium. *Biomaterials* **2008**, *29*, 161–171. [[CrossRef](#)]
21. Kokubo, T.; Kim, H.-M.; Kawashita, M. Novel bioactive materials with different mechanical properties. *Biomater.* **2003**, *24*, 2161–2175. [[CrossRef](#)]
22. Seong, W.-J.; Kim, U.-K.; Swift, J.Q.; Heo, Y.-C.; Hodges, J.S.; Ko, C.-C. Elastic properties and apparent density of human edentulous maxilla and mandible. *Int. J. Oral Maxillofac. Surg.* **2009**, *38*, 1088–1093. [[CrossRef](#)]
23. Lorna, J.G.; Ashby, M.F. *Cellular Solids; Structure and Properties*, 2nd ed.; Cambridge University Press: Cambridge, UK, 1988.
24. Rice, R.W. Evaluation and extension of physical property-porosity models based on minimum solid area. *J. Mater. Sci.* **1996**, *31*, 102–118. [[CrossRef](#)]
25. Kashef, S.; Asgari, A.; Hilditch, T.B.; Yan, W.; Goel, V.K.; Hodgson, P.D. Fracture toughness of titanium foams for biomedical applications. *Mater. Sci. Eng. A* **2010**, *527*, 7689–7693. [[CrossRef](#)]
26. Ghidelli, M.; Sebastiani, M.; Johannas, K.E.; Pharr, G.M. Effects of indenter angle on micro-scale fracture toughness measurement by pillar splitting. *J. Am. Ceram. Soc.* **2017**, *100*, 5731–5738. [[CrossRef](#)]
27. Ohman, C.; Baleani, M.; Perilli, E.; Dall’Ara, E.; Tassani, S.; Baruffaldi, F.; Viceconti, M. Mechanical testing of cancellous bone from the femoral head: Experimental errors due to off-axis measurements. *J. Biomech.* **2007**, *40*, 479–484. [[CrossRef](#)] [[PubMed](#)]
28. Norman, T.L.; Vashishth, D.; Burr, D.B. Fracture toughness of human bone under tension. *J. Biomech.* **1995**, *28*, 309–320. [[CrossRef](#)]

